Research on Chemical Intermediates (2024) 50:625–638
https://doi.org/10.1007/s11164-023-05208-y

ORIGINAL ARTICLE

Influence of preparation effects on 10 wt. %CuO/MnO_x catalytic activity in the preferential oxidation of CO (CO-PROX)

Raziyeh Jokar[1,2] · Seyed Mehdi Alavi[1] · Mehran Rezaei[1] · Ehsan Akbari[1]

Received: 3 October 2023 / Accepted: 10 December 2023 / Published online: 8 January 2024

Abstract

This study focused on the preparation of 10wt% CuO/MnO_x catalysts using three different MnO_x supports synthesized via hydrothermal, mechanochemical, and solution combustion methods. The catalysts were evaluated for preferential oxidation of CO for hydrogen purification within a temperature range of 40–250 °C at a gas hourly space velocity of 30000 (ml/(h.g_{cat})). Characterization of the synthesized catalysts was carried out using X-ray diffraction, Brunauer–Emmett–Teller, H_2 temperature-programmed reduction (H_2-TPR), and scanning electron microscopy analyses. Results showed that the employed method for the preparation of the catalyst support significantly affects the reduction temperature and the oxidation state of the final catalysts. The 10 wt% Cu/Mn-CMB catalyst exhibited better reducibility, higher CO conversion at 100 °C (94%), and appropriate catalytic stability in the presence of H_2O and CO_2 compared to the other samples.

Keywords Hydrogen · Hydrothermal · Mechano-chemical · Solution combustion · CO-PROX

Introduction

Proton exchange membrane fuel cells (PEMFCs) are recognized as sustainable energy sources capable of addressing energy demands and providing an alternative to fossil fuels [1]. Currently, CO preferential oxidation (CO-PROX) is widely

✉ Seyed Mehdi Alavi
Alavi.m@iust.ac.ir

✉ Mehran Rezaei
mrezaei@iust.ac.ir

[1] Chemical, Petroleum and Gas Engineering Department, Iran University of Science and Technology, Tehran, Iran

[2] Biosystems Engineering Department, Auburn University, 200 Corley Building, Auburn, AL 36849, USA

employed as an economical and practical method for purifying hydrogen before it is supplied to PEMFCs [2, 3]. Steam reforming or autothermal reforming of hydrocarbons and alcohols are the most conventional methods for hydrogen production. However, the hydrogen produced by these processes often contains a high percentage of carbon monoxide, which must be reduced to less than 10 ppm; otherwise, the Pt anode of the fuel cell may be poisoned by CO [4, 5]. Conventional methods for eliminating CO from hydrogen-rich streams include the water gas shift reaction (WGS) followed by methanation or CO preferential oxidation [3]. The output stream of the water gas shift reactor contains at least 0.5–1% of CO, which can poison the Pt electrode of PEMFCs [6]. Various effective solutions exist for removing CO from an H2 stream. However, preferential oxidation of CO and selective CO methanation are the most conventional and efficient methods for PEMFC applications. The CO-PROX process has garnered significant attention because it successfully reduces the CO percentage to 10 ppm [2–7].

The catalysts employed in CO-PROX include precious metal catalysts, such as Pt, Au, Ru, and base metal-based catalysts, such as Cu and Co [7]. While precious metal-based catalysts exhibit high activity in the PROX reaction, their application is restricted by their high cost and limited accessibility [7, 8].

Among base metal catalysts, CuO-CeO_2 catalysts have been investigated as promising alternatives to noble metal catalysts due to their superior catalytic performance in CO-PROX, potentially attributed to the high oxygen storage capacity of ceria [4, 8–13]. Additionally, manganese oxide, as a transition metal oxide with an acceptable price, high electron storage capacity, superior activity in supplying oxygen, and a perfect redox cycle ($Mn^{2+/}Mn^{3+} \rightarrow Mn^{3+/}Mn^{4+}$), has garnered increased attention for application in CO-PROX catalysts [14, 15]. The incorporation of copper into manganese oxide has been shown to improve catalytic activity by enhancing active oxygen mobility [16–19]. In our previous work [20], we prepared CuO/α-MnO_2 catalysts with various copper weight percentages, and the results indicated that the 10 wt% CuO/α-MnO_2 catalyst achieved nearly complete CO conversion at 130 °C. In our recent work, we aimed to shift the CO conversion temperature zone to lower temperatures and enhance catalyst resistance in the presence of water and carbon dioxide. It has been demonstrated that CO-PROX is a structure-sensitive reaction [4, 21], underscoring the importance of creating an effective catalytic structure for a highly active and stable catalyst.

Several methods have been employed to prepare CO-PROX catalysts, including sol–gel [22], deposition–precipitation (DP) [23], co-precipitation [24], solvent-free combustion [4], reflux [16], incipient wetness impregnation [25], mechanical mixing [26], and hydrothermal [20] methods. While sol–gel, DP, co-precipitation, reflux, incipient wetness impregnation, and hydrothermal methods are conventional routes, solvent-free combustion and mechanochemical methods are considered unconventional for CO-PROX catalyst preparation. Despite their unconventional status for CO-PROX, other researchers have successfully utilized these methods for the synthesis of manganese oxide catalysts in various oxidation processes, deeming them suitable routes. For instance, Akbari et al. [27] achieved success in preparing BaO-MnOx mixed oxide catalysts for low-temperature methane catalytic combustion using the eco-friendly mechanochemical method. Their

study demonstrated that the catalysts exhibited high catalytic activity. In a similar vein, Piumetti et al. [28] synthesized three different types of mesoporous manganese oxide catalysts for the total oxidation of volatile organic compounds (VOCs) through the solution combustion synthesis.

Mechanochemical synthesis, recognized as a green method, can be executed at room temperature [29, 30]. Renowned for its high speed and efficiency, this method requires fewer processing steps. Nanomaterials produced through mechanochemical synthesis exhibit unique characteristics, including a small crystallite size, uniform shape, and morphology with minimal agglomeration [31, 32]. Consequently, the mechanochemical approach has garnered significant attention due to its simple experimental equipment, the use of readily available precursors, and rapid, straightforward preparation steps [33, 34]. Another synthesis method, solution combustion synthesis (SCS), stands out in comparison to traditional preparation techniques. Catalysts prepared using SCS can be categorized as either bulk or supported catalysts [35]. Major SCS precursors include metal nitrates and an organic fuel (such as urea or glycine). The dissolved metal salt precursors and organic fuel in water undergo drying and heating, leading to a highly exothermic reaction and the formation of a porous powder [36]. Notably, this method offers the advantage of modifying the structure and morphology of the catalyst by adjusting preparation factors like calcination temperature and precursors' molar ratio [28, 36]. In this study, manganese oxide supports were prepared through hydrothermal, mechanochemical, and solution combustion routes. Subsequently, these supports were utilized in the preparation of 10 wt% CuO/MnOx catalysts for the CO-PROX process.

Experimental section

Catalysts preparation

The prepared catalysts were designated according to their respective preparation methods: 10Cu/Mn-HYD for hydrothermal, 10Cu/Mn-MCH for mechanochemical, and 10Cu/Mn-CMB for solution combustion methods. The synthesis procedures for 10Cu/Mn-HYD [20] and 10Cu/Mn-MCH [27, 37] supports were based on the methods described in our previous work. The MnO_x-CMB [38], preparation procedure is outlined as follows:

Manganese (II) nitrate tetrahydrate ($Mn(NO_3)_2.4H_2O$) and glycine ($C_2H_5NO_2$) with a glycine/metal nitrate molar ratio of 2 were dissolved in 50 ml of deionized water and stirred for 30 min. The solution was then heated at 100 °C until complete water evaporation. The resulting dried gel was transferred into an aluminum bowl and heated at 600 °C for 20 min. Subsequently, all three prepared supports underwent calcination at 500 °C for 3 h. Catalysts containing 10 wt% CuO supported on MnO_x-HYD, MnO_x-MCH, and MnO_x-CMB were prepared using the incipient wetness impregnation method. They were then calcined at 300 °C for 3 h before being employed in the CO-PROX reaction.

Catalyst characterizations

To determine the specific surface area (SBET) and pore characteristics of the catalysts, N_2 adsorption/desorption analysis was conducted at 77 K using a BELSORP-mini II analyzer. Prior to analysis, the samples underwent degassing at 250 °C for 2 h to eliminate moisture and other impurities. X-ray diffraction (XRD) analysis was performed using a PANalytical X'pert-Pro apparatus with a Cu-Kα radiation source (λ = 1.5486 Å) in the range of 10 to 80 degrees to identify the crystal phases of the calcined catalysts. Additionally, the average crystallite sizes of the calcined catalysts were calculated using the Scherrer equation (Eq. 1).

$$D = \frac{0.9\lambda}{\beta \cos \theta} \tag{1}$$

To investigate the reduction characteristics of the calcined catalysts, temperature-programmed reduction (TPR) analysis was conducted using a gas chromatograph device equipped with a thermal conductivity detector (TCD). For the TPR analysis, 25 mg of the calcined catalysts underwent pre-treatment at 250 °C for 2 h and were then cooled down to room temperature. Subsequently, the samples were exposed to a gas flow containing 5% H_2 in Ar (20 ml/min), with the temperature gradually increasing from room temperature to 600 °C at a ramp rate of 10 °C/min. Morphological studies of both the fresh and spent catalysts were carried out using a MIRA3 TESCAN instrument through scanning electron microscopy (SEM) analysis.

Activity tests

To assess the catalytic activity of CuO/MnO_x, a fixed-bed tubular quartz reactor was employed under atmospheric pressure within a temperature range of 40–250 °C. Before the reaction, 200 mg of the fresh sample was placed in the middle of the reactor and reduced with a pure H_2 gas stream (30 ml/min) at 180 °C for 2 h. Following this reduction step, the reactant gas stream, composed of 4% O_2, 4% CO, and 60% H_2 balanced with Ar, was introduced into the reactor. To mimic the conditions of a real CO-PROX process, 10% H_2O and 10% CO_2 were added to the feed stream. Product gases were monitored using an online gas chromatograph (Younglin, YL 6100) equipped with a micro thermal conductivity detector and a Carboxen 1010 column. CO conversion (XCO) and CO_2 selectivity (SCO_2) were determined using the following equations:

$$\text{CO conversion} = \frac{[CO]_{in} - [CO]_{out}}{[CO]_{in}} \times 100 \tag{2}$$

$$CO_2 \text{ selectivity} = \left[\frac{[CO]_{in} - [CO]_{out}}{[O_2]_{in} - [O_2]_{out}} \times 0.5 \right] \times 100 \tag{3}$$

Results and discussion

Structural properties and morphology of the calcined MnO_x catalysts

The N_2 adsorption–desorption isotherms and pore size distribution curves of calcined MnO_x samples are illustrated in Fig. 1a, b, respectively. According to Fig. 1a, the samples exhibited a type IV isotherm with an H3-type hysteresis loop [20]. Based on the IUPAC classification nonporous or macroporous inkbottle-shaped pore structure exists in the synthesized catalysts. The H3 type hysteresis formed when the neck size distribution is wide compared with the pore cavity size distribution [39]. The MnO_x-MCH hysteresis loop was in higher relative pressure (P/P0 = 0.8–1) range than the other ones, indicating the formation of larger pores in this sample. Figure 1b displays the pore size distribution of the MnO_x-HYD, MnO_x-MCH, and MnO_x-CMB samples. MnOx-HYD exhibited a pore size distribution spanning 2–45 nm, featuring mesopores within its structure. In contrast, both MnOx-MCH and MnOx-CMB displayed a combination of meso- and macropores. Specifically, MnOx-MCH revealed two peaks primarily at 15 nm and 30 nm. Conversely, MnOx-HYD revealed distribution peaks at a lower 10 nm and a main peak at 20 nm,

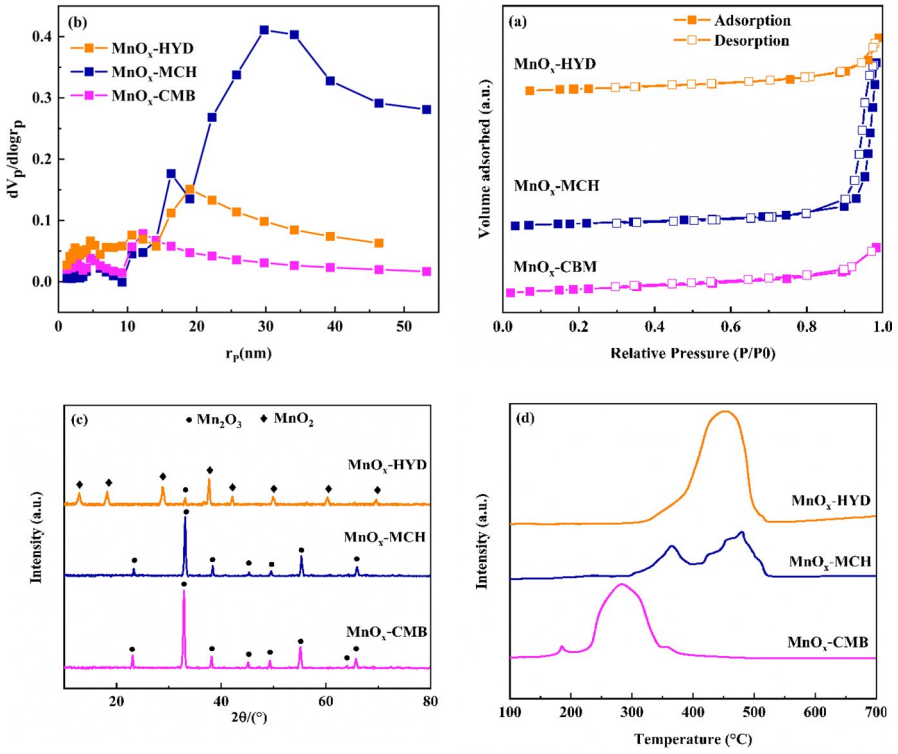

Fig.1 **a** N_2 isotherms, **b** pore size distributions, **c** XRD profiles, and **d** H_2-TPR analysis of supports

indicating a smaller pore distribution [40]. Referring to Table 1, it is evident that the MnOx-MCH sample, among the prepared samples, possessed the lowest BET area. The observed increase in specific surface areas can be attributed to the emergence of new and smaller pores, as elucidated by the pore size distribution [41].

The XRD patterns of the MnO_x samples with different preparation methods are mentioned in Fig. 1c. As noticed, all the diffraction peaks in MnO_x-HYD, MnO_x-MCH, and MnO_x-CMB samples are related to the MnO_2 [PDF-ICCD 44–0141] and Mn_2O_3 [PDF-ICCD41-1442] crystalline phases [42]. For the MnO_x-HYD, the MnO_2 crystalline phase formed while the other samples showed the Mn_2O_3 pattern as their main crystalline phase. The crystal sizes of the prepared catalysts are detailed in Table 1. As can see, the crystal size of the manganese oxide prepared by the hydrothermal method is smaller than the other samples, which confirms that the synthesis method affects the crystalline structure of the sample. Drawing from the literature [36, 43], the catalysts synthesized at elevated temperatures exhibited more pronounced crystalline structures compared to those synthesized at lower temperatures. The presence of glycine in the solution combustion synthesis method intensified the exothermic reaction, resulting in materials characterized by an increased average crystalline size. Notably, samples comprising the Mn_2O_3 phase displayed higher crystallinity than those containing the MnO_2 phase. This observation indicates varying enthalpies of formation, reflecting the presence of different phases in this case [36].

The redox features of the fresh supports were investigated by H_2-TPR analysis, and the outcomes are revealed in Fig. 1d. The reduction of the manganese oxides can be presented as follows: $MnO_2 \rightarrow Mn_2O_3 \rightarrow Mn_3O_4 \rightarrow MnO$ [20, 44]. As noticed in Fig. 1d each TPR curves of as-prepared support displays two or three main reduction peaks that can be related to the reduction of menagnese species in various valence conditions. Overall, the reduction peaks in the temperature ranges from 270 to 370 °C can be allocated to the reduction of MnO_2 to Mn_2O_3 and Mn_2O_3 to Mn_3O_4. Also, the peak appeared at 370 to 460 °C can be determined as a reduction of Mn_3O_4 to MnO [36]. The TPR results showed that the MnOx-CMB possessed the lowest reduction temperature and no reduction peak was distinguished at temperature higher than 400 °C. A small shoulder was discovered in the TPR profile of MnOx-HYD below 400 °C along with a main reduction peak centered around 450 °C. For the MnOx-MCH sample two main reduction peaks were observed at 350 and 470 °C, which are related to the reduction of $MnO_2 \rightarrow Mn_2O_3 \rightarrow Mn_3O_4$ and $Mn_3O_4 \rightarrow MnO$, respectively [36, 45]. According to the findings [46, 47], a low reduction temperature indicates a catalyst with sufficient oxygen vacancies, enabling

Table 1 Textural features of the MnO_x-HYD, MnO_x-MCH, and MnO_x-CMB supports calcined at 500 °C

Catalyst	S_{BET} ($m^2\ g^{-1}$)	Pore volume ($cm^3\ g^{-1}$)	Pore size (nm)	Crystal size (nm)
Mn-HYD	27.04	0.07	10.45	32.1
Mn-MCH	23.86	0.19	32.96	36.8
Mn-CMB	26.98	0.05	8.86	38.2

it to effectively reduce oxygen even under conditions of low thermal energy. This characteristic enhances the catalyst's usability, allowing for more efficient oxygen utilization compared to alternative catalysts. Consequently, this promotes the creation of active species, contributing to an outstanding catalytic performance.

Structural properties of the copper doped MnO_x catalyst

Figure 2a, b showed the N_2 adsorption–desorption isotherms and BJH pore size distribution curves of the three different 10 wt% Cu/Mn catalysts. The results revealed that the incorporation of copper into the catalyst support, coupled with the calcination step, induced changes in the structural features and morphology of the catalysts. As shown in Fig. 2a, all samples exhibited a type IV isotherm with an H3-type hysteresis loop [20], consistent with the meso/macro-porous structure present in the synthesized catalysts [44]. Compared to the supports, the 10Cu/Mn-HYD and 10Cu/Mn-MCH catalysts exhibited a smaller pore size distribution while the 10Cu/Mn-CMB catalyst possesset the broadest pore size distribution (Fig. 2b). Textural properties of the 10Cu/Mn-HYD, 10Cu/Mn-MCH, and 10Cu/Mn-CMB illustrated in Table 2. As can be seen, the addition of

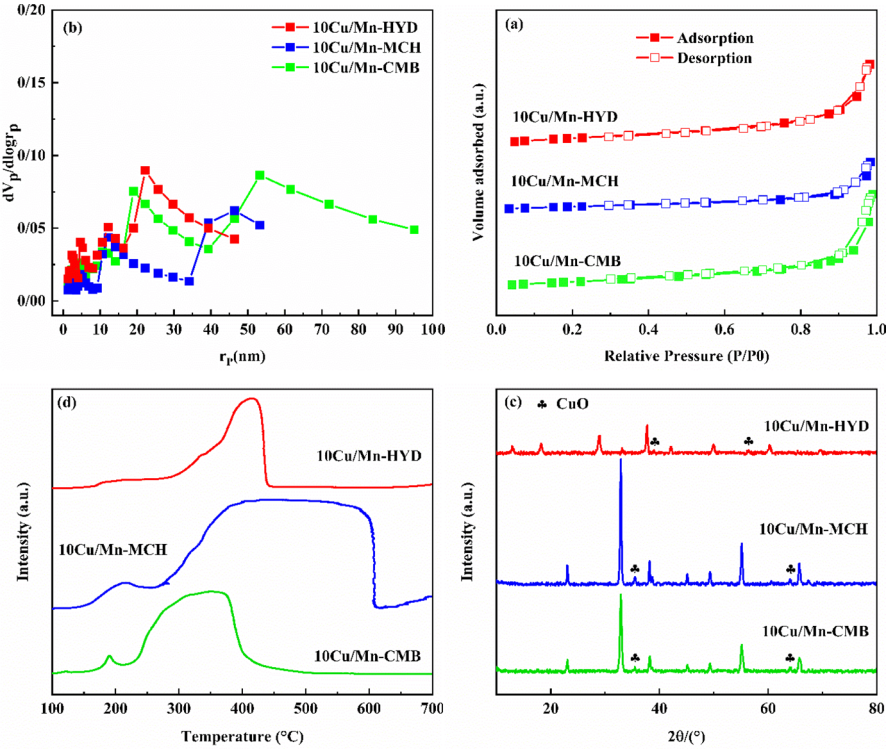

Fig.2 **a** N_2 isotherms, **b** pore size distributions, **c** XRD profiles, and **d** H_2-TPR analysis of catalysts

Table 2 Textural features of the 10Cu/Mn-HYD, 10Cu/Mn-MCH, and 10Cu/Mn-CMB catalysts calcined at 300 °C

Catalyst	S_{BET} ($m^2\ g^{-1}$)		Pore volume ($cm^3\ g^{-1}$)		Pore size (nm)		Crystal size (nm)
	fresh	spent	fresh	spent	fresh	spent	
10Cu/Mn-HYD	25.18	20.3	0.06	0.05	10.63	9.5	31.7
10Cu/Mn-MCH	11.99	11.2	0.03	0.03	13.06	13.85	44.5
10Cu/Mn-CMB	22.45	21.97	0.07	0.07	13.57	14.43	36.8

copper to the as-prepared supports diminished the surface area of the catalysts due to the occupation of some pores during the impregnation of copper [48]. The 10Cu/Mn-HYD displayed the highest BET area while the 10Cu/Mn-MCH sample demonstrated considerable surface decrement. The 10Cu/Mn-CMB showed the greatest pore volume and pore size compared to other samples.

To investigate crystalline phase behavior of as-prepared samples, XRD analysis reported in Fig. 2c. The impregnation of 10 wt% copper oxides to the MnO_x-HYD, MnO_x-MCH, and MnO_x-CMB supports caused the formation of CuO phases. The copper oxide crystalline phases were assigned based on [JCPDS 80–0076 or JCPDS05-0661] [20, 49].

The H_2-TPR profiles of the catalysts are illustrated in Fig. 2d. As expected, the addition of copper oxide to the catalyst supprt affected the reduction charactrestics of the catalyst support.

The copper oxide reduction peak was observed at about 200 °C, which is related to the single-step reduction of the copper oxide ($Cu^{2+} \rightarrow Cu^0$) [10]. The manganese oxide was reduced in a wide temperature range. For the 10Cu/Mn-HYD, and 10Cu/Mn-CMB samples the reduction peak of the manganese oxide was observed at temperature lower than 450 °C. However, in 10Cu/Mn-MCH reduction peak was shifted to higher temperature. It means that the reduction of $Cu^{2+}/Mn^{4+} \rightarrow Cu^{+}/Mn^{3+}$ and then $Cu^{+}/Mn^{3+} \rightarrow Cu^{0}/Mn^{2+}$ must be more difficult in 10Cu/Mn-MCH than 10Cu/Mn-HYD and 10Cu/Mn-CMB samples. Moreover, Dang et al. [41], indicated that the presence of copper contributes to improving the reducibility of manganese oxide through the hydrogen effect, with a significant reliance on the well-dispersed CuO. As a result, the choice of various synthesis methods for support significantly impacts the redox characteristics of the catalyst [9].

Figure 3 illustrates the SEM images of the 10Cu/Mn-HYD, 10Cu/Mn-MCH, and 10Cu/Mn-CMB samples. The 10Cu/Mn-HYD catalyst exhibited a nanowire structure, while the 10Cu/Mn-MCH catalyst displayed agglomerate spherical particles (Fig. 3b). Conversely, the 10Cu/Mn-CMB catalyst exhibited a sponge-like structure characterized by high porosity and aggregated particles.

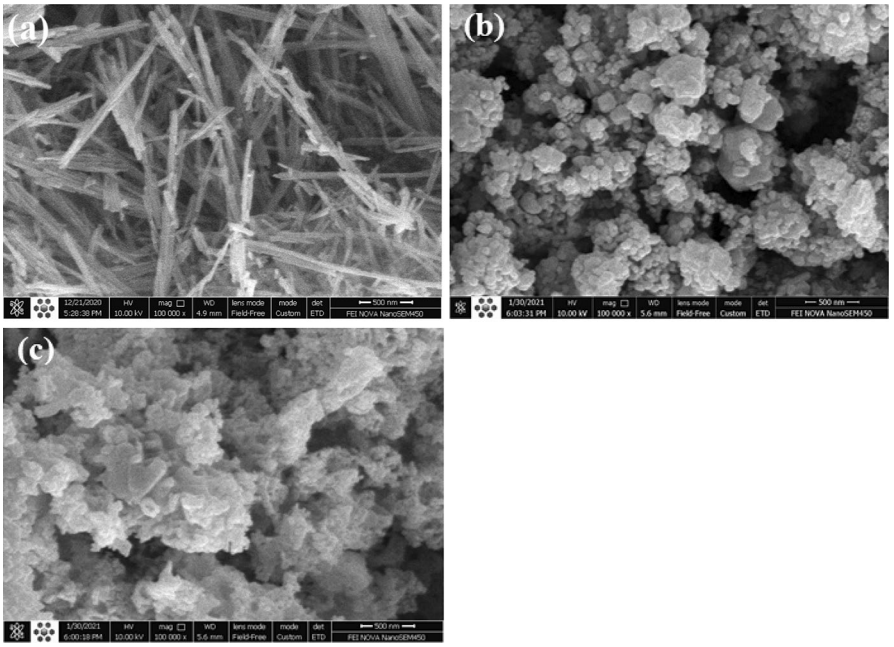

Fig.3 SEM analysis of **a** 10Cu/Mn-HYD, **b** 10Cu/Mn-MCH, and **c** 10Cu/Mn-CMB catalysts

Activity of 10 wt. %CuO/MnO_x catalysts

According to Fig. 4, the catalysts' performance was assessed based on two criteria: conversion and selectivity. Across all samples, the elevation of the reaction temperature induced the formation of Cu^+ species, identified as the primary active species in the CO-PROX reaction [11]. Notably, the 10Cu/Mn-CMB catalyst exhibited the highest CO conversion rate (94%) at 100 °C, attributed to its low reduction temperature. The occurrence of Cu^+ species at lower temperatures

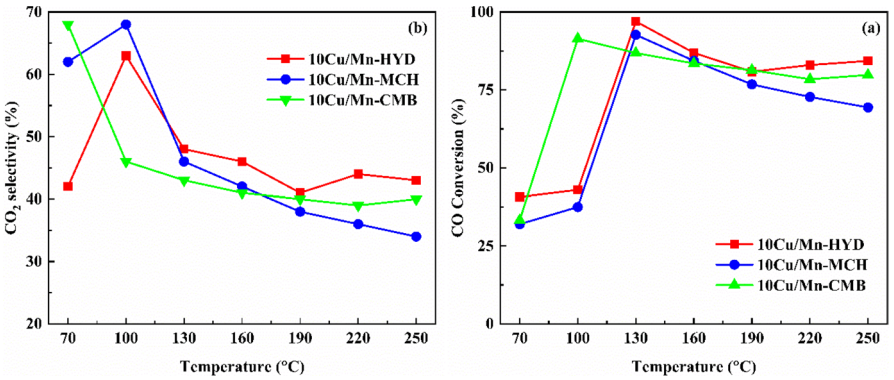

Fig.4 **a** CO conversion and **b** CO_2 selectivity of catalysts

is a recognized outcome of reduced reduction temperatures [50]. Interestingly, increasing the reaction temperature to 130 °C resulted in altered CO conversion patterns among the catalysts, with the sequence being 10Cu/Mn-HYD > 10Cu/Mn-MCH > 10Cu/Mn-CMB.

CO_2 selectivity of all catalysts consistently maintains an average value of 50%, a level deemed acceptable for ensuring effective CO-PROX catalytic performance in the presence of excess oxygen [41]. However, as the temperature increases, a discernible downward trend is observed in the CO_2 selectivity of Cu/Mn catalysts. This phenomenon can be attributed to the enhanced oxidation rate of H_2 at elevated temperatures. The resulting production of water as a byproduct poses an impediment to reactant adsorption on the catalyst surface, thereby influencing the occurrence of the CO oxidation reaction [41, 48].

To evaluate the performance of the as-prepared catalysts in a realistic PROX reaction scenario, we introduced 10% CO_2 and 10% H_2O into the feed composition, presenting the findings in Fig. 5. Consistent with prior research [11, 16, 45, 50], the actual PROX feed stream introduces an inhibitory influence on CO conversion and CO_2 selectivity. The introduction of H_2O and CO_2 in the feedstream is observed to shift the conversion temperatures of all catalysts to higher values, significantly narrowing the acceptable temperature window for CO conversion [51]. The presence of CO_2 induces the formation of stable carbonates due to reduced manganese species, strongly inhibiting CO conversion. However, at higher temperatures, these carbonates may transform into less stable species, mitigating deactivation by unblocking copper sites and thereby positively influencing catalytic performance, as suggested by Cruz. Additionally, the introduction of H_2O leads to the chemisorption of water molecules on the catalyst's active sites [52]. Notably, the 10Cu/Mn-CMB catalyst exhibits outstanding performance under actual PROX conditions, a merit attributed to a larger quantity of easily reducible copper oxide species that strongly interact with manganese. Nevertheless, it is noteworthy that the other two samples, characterized by closely aligned pore size distribution patterns and similar reduction behaviors, exhibited similar

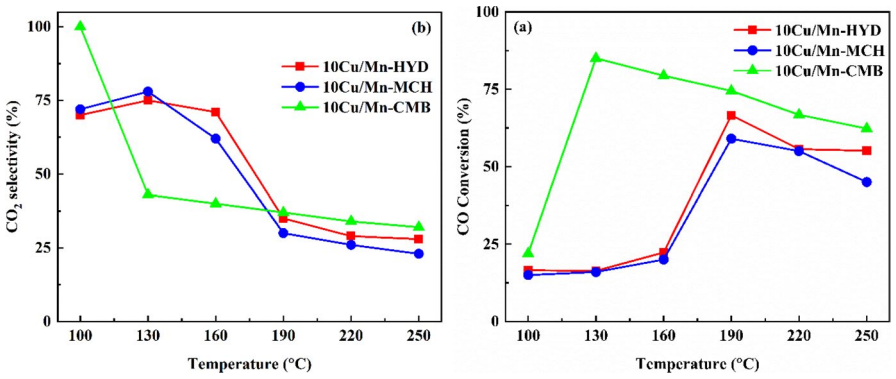

Fig.5 Impact of the presence of 10% H_2O and 10% CO_2 in the feed stream on the **a** CO conversion and **b** CO_2 selectivity

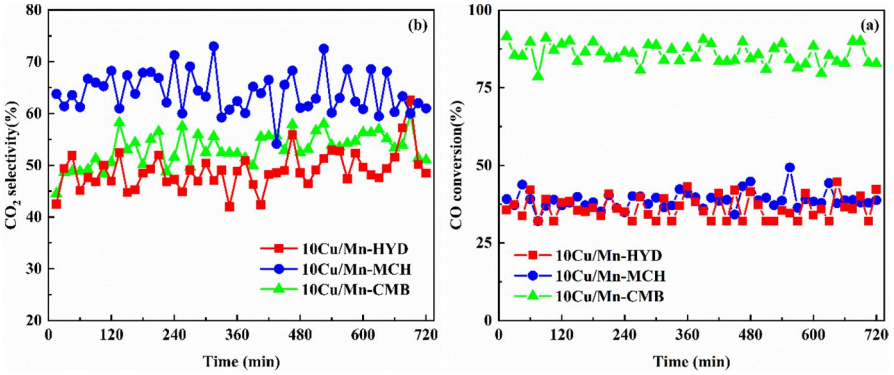

Fig.6 Long-term stability test of catalysts. Reaction conditions: 4% CO, 4% O_2, 60% H_2 balanced with Ar: GHSV = 30000(ml/h.g_{cat})

catalytic performances. Therefore, unique morphology and porosity of the 10Cu/Mn-CMB, including the presence of macropores, contribute significantly by minimizing active site blockage caused by H_2O [11].

Catalytic stability test and SEM

Catalyst stability is a critical factor in determining catalyst efficiency. Figures 6 and 7 present the catalytic stability and SEM images of the spent samples after 12 h of the PROX reaction at 100 °C, respectively. As observed in Fig. 6a, b, the CO conversion and CO_2 selectivity of each sample exhibit fluctuations of about 10%, with none of them showing a significant drop during the test. This observation is further confirmed by Fig. 7a–c, where the morphologies of the samples remain unchanged after the stability test.

Conclusion

The 10Cu/Mn-HYD, 10Cu/Mn-MCH, and 10Cu/Mn-CMB catalysts were synthesized using hydrothermal, mechanochemical, and solution combustion methods, respectively, and the calcined samples were evaluated for the CO-PROX reaction. While the 10Cu/Mn-CMB exhibited the best performance at 100 °C with 94% CO conversion, the 10Cu/Mn-HYD demonstrated superior activity at higher temperatures, achieving nearly 100% CO conversion at 130 °C. Under real feed conditions for all samples, the CO_2 selectivity remained stable at around 50%. Notably, the 10Cu/Mn-CMB outperformed the others with 85% CO conversion at 100 °C, attributed to its lower temperature reducibility and macroporous structure.

Acknowledgements This work was supported by the Iran National Science Foundation (INSF) under the grant number of 97017638.

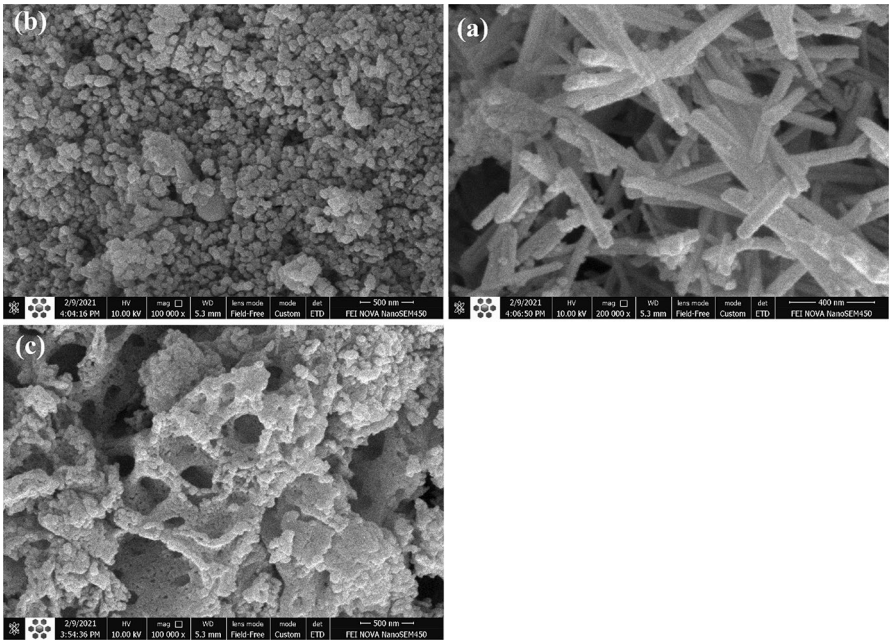

Fig.7 SEM analysis of 10Cu/Mn-HYD, 10Cu/Mn-MCH, and 10Cu/Mn-CMB catalysts after long-term stability test

Author contributions CRediT authorship contribution statement: Raziyeh Jokar: Conceptualization, Data Curation, Formal analysis, Investigation, methodology, writing – original Draft, review & editing. Seyed Mehdi Alavi: Conceptualization, Methodology, Resources, Funding acquisition, Validation, review & edit. Mehran Rezaei: Conceptualization, Methodology, Resources, Funding acquisition, Validation, review & edit. Ehsan Akbari: Conceptualization, Validation, review & edit.

Declarations

Competing interests The authors declare no competing interests.

References

1. SS. Kumar, V. Himabindu, Hydrogen production by PEM water electrolysis – A review (2019)
2. L. Zhong, M. Barreau, D. Chen, V. Caps, M. Haevecker, D. Teschner, D.H. Simonne, E. Borfecchia, W. Baaziz, B. Šmíd, S. Zafeiratos, Appl. Catal. B Environ. **27**, 120397 (2021)
3. L. Ilieva, P. Petrova, G. Pantaleo, R. Zanella, J.W. Sobczak, W. Lisowski, I. Ivanov, Z. Kaszkur, L.F. Liotta, A.M. Venezia, Tabakova T. **357**, 547 (2020)
4. Y. Zhao, K. Chen, Q. Zou, J. Fang, S. Zhu, S. He, J. Lu, Y. Luo, J. Power Sour. **484**, 229181 (2021)
5. D.B. Pal, R. Chand, S.N. Upadhyay, P.K. Mishra, Renew. Sustain. Energy Rev. **93**, 549 (2018)
6. A.M. Lacoste, I.S. Tiscornia, M. Bonne, L. Michelin, B. Lebeau, A.V. Boix, Microporous Mesoporous Mater. **320**, 111094 (2021)
7. X. Dong, L. Guo, C. Wen, N. Ren, Z. Cao, N. Liu, L.L. Guo, Res. Chem. Intermed. **41**, 10049 (2015)

8. S. Malwadkar, P. Bera, C.V. Satyanarayana, J. Rare Earths **38**(9), 941 (2020)
9. Y. Xie, J. Wu, G. Jing, H. Zhang, S. Zeng, X. Tian, X. Zou, J. Wen, H. Su, C.J. Zhong, P. Cui. **239**, 665 (2018)
10. M. Monte, D. Gamarra, A.L. Cámara, S.B. Rasmussen, N. Gyorffy, Z. Schay, A. Martínez-Arias, J.C. Conesa, Preferential oxidation of CO in excess H2 over CuO/CeO2 catalysts: Performance as a function of the copper coverage and exposed face present in the CeO2 support (2014)
11. J.A. Cecilia, A. Arango-Díaz, J. Marrero-Jerez, P. Núñez, E. Moretti, L. Storaro, E. Rodríguez-Castellón. **7**(5), 160 (2017)
12. G. Jing, X. Zhang, A. Zhang, M. Li, S. Zeng, C. Xu, H. Su, Appl. Surface Sci. **434**, 445 (2018)
13. A.R. Cruz, E.M. Assaf, J.F. Gomes, J.M. Assaf, J. Environ. Manag. **242**, 272 (2019)
14. Y.A. May, S. Wei, W.Z. Yu, W.W. Wang, C.J. Jia, Langmuir **36**(38), 11196 (2020)
15. Z. Zhang, Y. Tian, W. Zhao, P. Wu, J. Zhang, L. Zheng, T. Ding, X. Li, Catal. Today **355**, 214 (2020)
16. A. Davo-Quinonero, I. Such-Basanez, J. Juan-Juan, D. Lozano-Castello, P. Stelmachowski, G. Grzybek, A. Kotarba, A. Bueno-Lopez. **267**, 118372 (2020)
17. E.C. Njagi, H.C. Genuino, C.K. King'ondu, C.H. Chen, D. Horvath, S.L. Suib, Int. J. Hydrog. Energy **36**(11), 6768 (2011)
18. A. Elmhamdi, L. Pascual, K. Nahdi, A. Martínez-Arias. **217**, 1 (2017)
19. A. Davó-Quiñonero, M. Navlani-García, D. Lozano-Castello, A. Bueno-López. **6**(14), 5684 (2016)
20. R. Jokar, S.M. Alavi, M. Rezaei, E. Akbari. **46**(64), 32503 (2021)
21. C. Wang, Q. Cheng, X. Wang, K. Ma, X. Bai, S. Tan, Y. Tian, T. Ding, L. Zheng, J. Zhang, X. Li, Appl. Surface Sci. **422**, 932 (2017)
22. A. Manasilp, E. Gulari. **37**, 17 (2002)
23. S. Chayaporn, C. Thunyaratchatanon, A. Luengnaruemitchai. **46**, 4173 (2020)
24. X. Han, L. Gou, S. Tang, F. Cheng, M. Zhang, M. Guo. **283**, 111941 (2021)
25. P. Jing, X. Gong, B. Liu, J. Zhang. **10**(4), 919 (2020)
26. H. Choi, J. Kim, S.J. Choung, J. Kim, M.R. Othman, Chem. Eng. Sci. **172**, 688 (2017)
27. R. Jokar, S.M. Alavi, M. Rezaei, E. Akbari. **48**(64), 24833 (2022)
28. M. Piumetti, D. Fino, N. Russo. **163**, 277 (2015)
29. S. Kazemi, S.M. Alavi, M. Rezaei. **47**, 18370 (2022)
30. K. Tamimi, S.M. Alavi, M. Rezaei, E. Akbari. **99**, 48 (2021)
31. S. Gholami, S.M. Alavi, M. Rezaei. **46**, 5311 (2021)
32. M. Ahadzadeh, S.M. Alavi, M. Rezaei, E. Akbari. **524**, 112325 (2022)
33. M. Varbar, S.M. Alavi, M. Rezaei, E. Akbari. **48**, 1129 (2022)
34. P. Shafiee, S.M. Alavi, M. Rezaei. **46**, 3933 (2021)
35. A. Varma, A.S. Mukasyan, A.S. Rogachev, K.V. Manukyan, Chem. Rev. **116**(23), 14493 (2016)
36. S. Andreoli, F.A. Deorsola, C. Galletti, R. Pirone. **278**, 174 (2015)
37. S. Sabokmalek, S.M. Alavi, M. Rezaei, E. Akbari. **153**, 3698 (2023)
38. T. Kumaresh, E.W. Awin, L.K. Bhaskar, M.P. Djordjevic, B. Matović, R. Kumar, J. Solid State Chem. **302**, 122420 (2021)
39. K.A. Cychosz, M. Thommes. **4**(4), 559 (2018)
40. H. Pordelan, S.M. Alavi, M. Rezaei, E. Akbari. **153**(10), 3159 (2023)
41. H. Dang, W. Zhao, R. Wu, L. Yue, Y. Wang, Z. Ren, Y. Zhao, Int. J. Hydrog. Energy **48**, 27619 (2023)
42. E. Akbari, S.M. Alavi, M. Rezaei, A. Larimi. **60**(20), 7572 (2021)
43. T.S. Lazarova, D. Kovachevaa, M. Georgieva, D. Tzankov, G. Tyuliev, I. Spassova, A. Naydenov, Appl. Surface Sci. **496**, 143571 (2019)
44. E. Akbari, S.M. Alavi, M. Rezaei, A. Larimi. **47**, 13004 (2022)
45. M. Andache, A.N. Kharat, M. Rezaei, Int. J. Hydrog. Energy **44**, 27401 (2019)
46. W. Dai, Z. Li, C. Li, C. Zhang, F. Wang, P. Liu, H. Qiao, J. Ind. Eng. Chem. **121**, 15 (2023)
47. D.H. Kim, Y.J. Park, K.Y. Lee, H.P. Ha, D.W. Kwon, Appl. Catal. A: Gen. **643**, 118770 (2022)
48. Y. Xing, J. Wu, C. Zhang, L. Zhang, J. Han, D. Liu, H. Wang, X. Hou, Z. Gao. **48**, 20667 (2023)
49. A. Martínez-Arias, D. Gamarra, A.B. Hungría, M. Fernández-García, G. Munuera, A. Hornés, P. Bera, J.C. Conesa, A.L. Cámara, Catalysts **3**(2), 378 (2013)
50. A. Davó-Quiñonero, D. Lozano-Castello, A. Bueno-López, Appl. Catal. B Environ. **217**, 459 (2017)

51. O.H. Laguna, M.I. Domínguez, S. Oraá, A. Navajas, G. Arzamendi, L.M. Gandía, M.A. Centeno, M. Montes, J.A. Odriozola, Catal. Today **203**, 182 (2013)
52. S. Adak, J. Rabeah, R. Ranjan, T.S. Khan, M.K. Poddar, R.K. Gupta, T. Sasaki, S. Kumar, A. Bordoloi, C.S. Gopinath, A. Brückner. **624**, 118305 (2021)